12-17-2008

Obtaining a Relationship Between Process Parameters and Fracture Characteristics for Hybrid CO2 Laser/Waterjet Machining of Ceramics

Dinesh Kalyanasundaram
Iowa State University, kdinesh@iastate.edu

Pranav Shrotriya
Iowa State University, shrotriy@iastate.edu

Palaniappa A. Molian
Iowa State University, molian@iastate.edu

Obtaining a Relationship Between Process Parameters and Fracture Characteristics for Hybrid CO_2 Laser/Waterjet Machining of Ceramics

Dinesh Kalyanasundaram[1]
e-mail: kdinesh@iastate.edu

Pranav Shrotriya
Binger Assistant Professor of Mechanical Engineering

Pal Molian

Laboratory for Lasers, MEMS and Nanotechnology,
Department of Mechanical Engineering,
Iowa State University,
Ames, IA 50014

A combined experimental and analytical approach is undertaken to identify the relationship between process parameters and fracture behavior in the cutting of a 1 mm thick alumina samples by a hybrid CO_2 laser/waterjet (LWJ) manufacturing process. In LWJ machining, a 200 W power laser was used for local heating followed by waterjet quenching of the sample surface leading to thermal shock fracture in the heated zone. Experimental results indicate three characteristic fracture responses: scribing, controlled separation, and uncontrolled fracture. A Green's function based approach is used to develop an analytical solution for temperatures and stress fields generated in the workpiece during laser heating and subsequent waterjet quenching along the machining path. Temperature distribution was experimentally measured using thermocouples and compared with analytical predictions in order to validate the model assumptions. Computed thermal stress fields are utilized to determine the stress intensity factor and energy release rate for different configurations of cracks that caused scribing or separation of the workpiece. Calculated crack driving forces are compared with fracture toughness and critical energy release rates to predict the equilibrium crack length for scribed samples and the process parameters associated with transition from scribing to separation. Both of these predictions are in good agreement with experimental observations. An empirical parameter is developed to identify the transition from controlled separation to uncontrolled cracking because the equilibrium crack length based analysis is unable to predict this transition. Finally, the analytical model and empirical parameter are utilized to create a map that relates the process parameters to the fracture behavior of alumina samples.
[DOI: 10.1115/1.3026547]

Keywords: CO_2 laser/waterjet (LWJ) machining, thermal shock, alumina, fracture, crack propagation, ceramic

1 Introduction

Structural ceramics, such as alumina (aluminum oxide), are widely used for a variety of applications ranging from microelectronics to prosthetics because of desirable properties such as high hardness, low chemical reactivity, high volume receptivity at elevated temperatures, low density, low thermal conductivity, and ultrafine finishing capability. Traditional cutting methods for structural ceramics are limited by their brittleness, high hardness, and low thermal expansion, leading to increased vulnerability to workpiece fracture, significant loss of workpiece material, tool failure, difficulty in achieving the design requirements of high precision and excellent surface integrity, and need for regular maintenance due to wear [1–7].

It is crucial to develop novel machining processes that can fabricate ceramic parts at a relativity high rate, while eliminating the fractures and breakages associated with current manufacturing methods [2,3]. CO_2 laser cutting is an accepted industrial technique for producing useful shapes in ceramics, such as alumina, due to its localized heating effect and noncontact nature over mechanical methods. However, it does not necessarily preclude damage and/or fracture of the workpiece due to uncontrolled cracking.

CO_2 laser cutting of ceramics can be accomplished by three different methods: (1) melting and evaporation where the melt layer is blown off by a high-pressure (80–90 psi) gas stream; (2) partial evaporation to form a deep groove followed by applying a mechanical force or ultrasonic energy to break the material; and (3) controlled thermal stress fracture where the laser energy produces thermal stress causing the material separation similar to a crack extension. The evaporation/melting mode of material removal requires extreme power lasers (>500 W), leading to collateral thermal damage such as residual stresses, heat affected zone, recast layer, uncontrolled fracture, etc. [5,7,8]. Mechanical score and snap methods also result in surface damage such as microcrack, residual stress, etc. In contrast, the controlled thermal stress fracture mode of material removal can be achieved at low powers (15–20 W) but suffers from slowness and a narrow range of process parameters.

Thermal shock fracture of brittle materials has been investigated for the last few decades. Lumley [9] was one of the earliest researchers to demonstrate the controlled thermal fracture of glass specimens using lasers. Controlled thermal shock fracture mechanism is an energy efficient process as low-powered lasers operating below the melt/ablation threshold are utilized for localized heating of the workpiece, and a gas stream is added for cooling

[1]Corresponding author.

Contributed by the Materials Division of ASME for publication in the JOURNAL OF ENGINEERING MATERIALS AND TECHNOLOGY. Manuscript received March 21, 2008; final manuscript received August 9, 2008; published online December 17, 2008. Assoc. Editor: Hamid Garmestani.

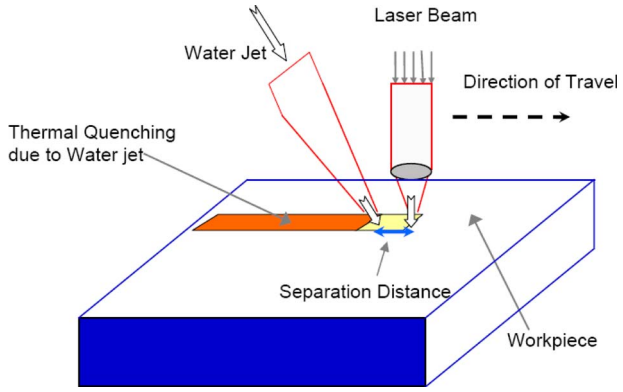

Fig. 1 Schematic representation of the laser/waterjet system

the heated zone, leading to fracture of the sample. Tsai and coworkers [10,11] demonstrated the thermal shock fracture mode for cutting alumina substrates. It was also observed that larger spot sizes help in the increase in cutting speed, as well as cut quality over traditional machining processes. Unfortunately, control of the fracture path necessitates the use of slow feed rates (~5–10 mm/s) (see Refs. [10,11]). In addition, the scattering errors associated with the process often promote uncontrolled crack propagation. Segall et al. [12] reported a dual-beam laser cutting process where one beam causes prescoring of the workpiece surface while the other beam fractures the sample [12]. Prescored groove on the sample surface serves to guide the thermal stress-induced crack. As compared to single beam controlled fracture machining, dual-beam machining produced a modest increase in the feed rate in the cutting of alumina (~150%) [12].

Previous analysis of alumina fracture during laser cutting have primarily relied on finite element analysis for prediction of thermal stresses [10,13–15], and localized melting in the workpiece has been modeled through the removal of nodes in the region where the temperature exceeded the alumina melting temperature [13,15]. Experimental observations of workpiece fracture are explained either by comparing the computed maximum tensile stress to alumina strength [10,13,14] or through empirical probabilistic measures based on computed stress fields [15]. These approaches are primarily suitable for the analysis of experimental observations and may not be suitable for identifying processing conditions for the controlled cutting of the alumina workpiece.

A combined experimental and computational approach is utilized to analyze crack propagation in the alumina workpiece during LWJ machining. A novel approach of combining laser and waterjet (see Fig. 1) was developed, and proof-of-concept studies on cut quality and energy efficiency in machining alumina were reported in our previous publications [5,7]. The laser heating creates a temperature gradient in a zone approximately equal to thermal diffusion depth, and rapid quenching of that zone by the waterjet develops thermal stresses that fracture this zone. As a result, LWJ machining allows higher feed rates and cleaner cuts. In addition, it avoids the formation of liquid and gaseous phases, making the cutting process more energy efficient and free from hazardous emission.

In this work, cutting experiments are conducted to identify typical process parameters that correspond to scribing, controlled separation, and uncontrolled fracture of the workpiece. An analytical model is developed for determining the transient temperature and stress distribution during laser heating and subsequent waterjet quenching. Measured thermal histories of samples during LWJ cutting are compared with model predictions to validate the thermal analysis and modeling assumptions. The experimentally validated model is used to compute driving forces for two different crack configurations: (i) plane strain crack, which a single dominant crack aligned with the through-thickness direction [16], and (ii) channeling, which is a crack aligned along the cutting direction [17,18]. Crack driving forces are compared with the fracture toughness of alumina to obtain a relationship between process parameters and workpiece fracture characteristics.

2 Experimental Procedure

Square plates of 96% alumina that were $100\times100\times1$ mm^3 in dimension were purchased from Coorstek (Golden, CO) and samples of 25×25 mm^2 were prepared for LWJ cutting experiments. Two different experiments are performed on alumina samples: The first set of experiments were used to determine the processing parameters that correspond to controlled separation, and the second set of experiments were used to record the temperature history of specimens during laser waterjet machining. A simple fixture was fabricated to hold the samples such that the area directly below the cutting path is not in contact with metallic surfaces to minimize heat transfer at the bottom surface (Fig. 2). The details of the hybrid laser waterjet cutting system are described in a previous publication [5].

2.1 Experiments on Machining of Alumina. LWJ experiments were conducted to investigate the effect of two process parameters—line energy (laser energy per unit cutting length) and surface energy density (laser energy per unit surface area)—on the fracture behavior of alumina samples. Different values of process parameters were achieved by varying the laser power from 100 W to 200 W and the cutting speed from 25 mm/s to 50 mm/s (60–120 in./min) and using two different laser spot sizes (0.6 mm (defocused beam) and 0.2 mm (focused beam)). Other process parameters, such as water pressure, distance of separation between the heating and the cooling zone, and waterjet nozzle size, were set at 2 MPa, 1.3 mm, and 0.3 mm, respectively.

2.2 Thermal History of Alumina Samples During LWJ cutting. Thermocouples were attached to alumina samples at offset distances of 1 mm, 2 mm, and 3 mm from the laser path (as schematically shown in the inset of Fig. 2) to record the temperature history during laser/waterjet cutting. The temperature was measured using K-type thermocouples with a 0.8 mm head diameter (Omega, PA) suitable to measure temperatures of up to 1250°C. A data acquisition system was used to record the temperature at a time interval of 0.5 s during the LWJ cutting.

3 Thermal Stress and Crack Driving Force Calculation

An analytical model is developed to predict the temperatures and stress fields in alumina samples undergoing laser/waterjet machining. Computed stress fields are subsequently used to obtain a relationship between the process parameters and driving forces for different configurations of cracks that lead to cutting/scribing of the workpiece.

3.1 Analytical solution of temperature and stress fields. Temperature distribution, $T(x,y,z,t)$, in the workpiece is determined by modeling the laser and waterjet as a rectangular source and sink [19], respectively, as shown schematically in Fig. 3, in order to simplify the analytical solutions. Transient temperature distributions are obtained by the solution of the following diffusion equations:

$$c_p\rho\frac{\partial T}{dt} = k\nabla^2 T + q(x,y,t,I_h,I_c)$$

$$\begin{aligned} q(x,y,t,I_h,I_c) = {} & I_h H(h_x - |x|)[H(vt-y) - H(vt-y-2h_y)] \\ & - I_c H(c_x - |x|)[H(vt-2h_y-l_0-y) \\ & - H(vt-2h_y-l_0-2c_y-y)] \end{aligned} \quad (1)$$

where c_p is the specific heat of the material, ρ is the density of the

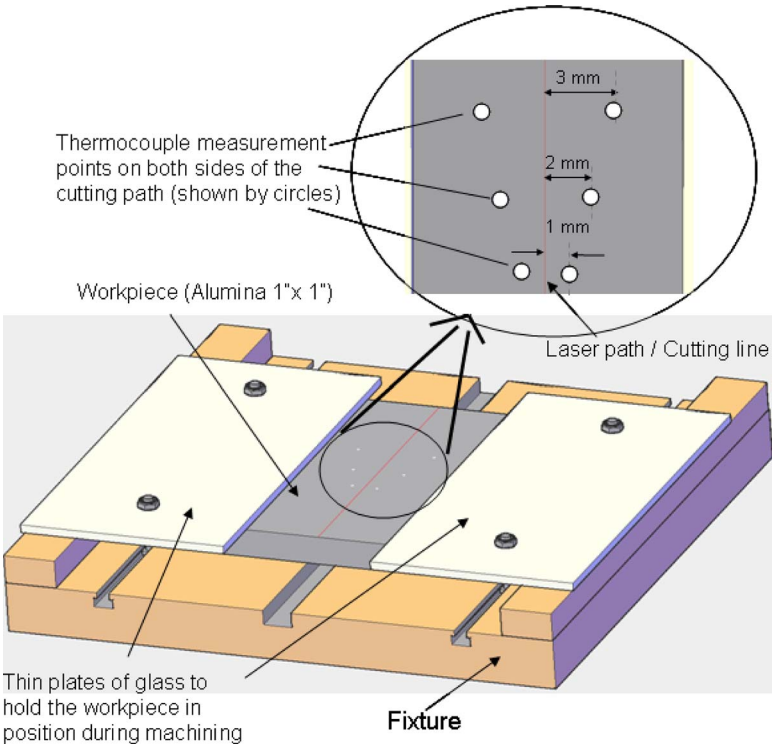

Fig. 2 Schematic representation of the fixture with the workpiece in position during machining. Inset shows the thermocouple measurement points for recording the temperature history.

material, k is the conductivity of the material, $q(x,y,t,I_h,I_c)$ is the total heat input, I_h is the heating intensity of the laser beam and I_c is the cooling intensity of the waterjet, H is the Heaviside function, v is the velocity of the cutting head, h_x, c_x, h_y, and c_y are the half lengths of the heating and cooling zones along the x and y directions, respectively, and l_0 is the separation distance between the laser spot and the waterjet cooling zone on the surface of the workpiece. Elperin et al. [19] previously reported an analytical solution for the temperature field using an error function representation that provides an elegant solution but leads to complicated and cumbersome expressions in the calculation of thermal stress distributions. In order to simplify the thermal stress calculation, we have used an eigenfunction expansion for the solution of the temperature fields.

Both the laser heating and waterjet cooling occurs on the top surface, and hence the convective heat transfer boundary conditions are used for the top surface. Insulated boundary conditions are used at the bottom surface. Convective heat transfer boundary conditions are used for all the side surfaces except $y=0$ mm (starting edge), which is modeled as an insulated surface, to simplify the analytical solution. As a result, initial and boundary conditions for the heat flow are

$$T(x,y,z,t=0)=T_0$$

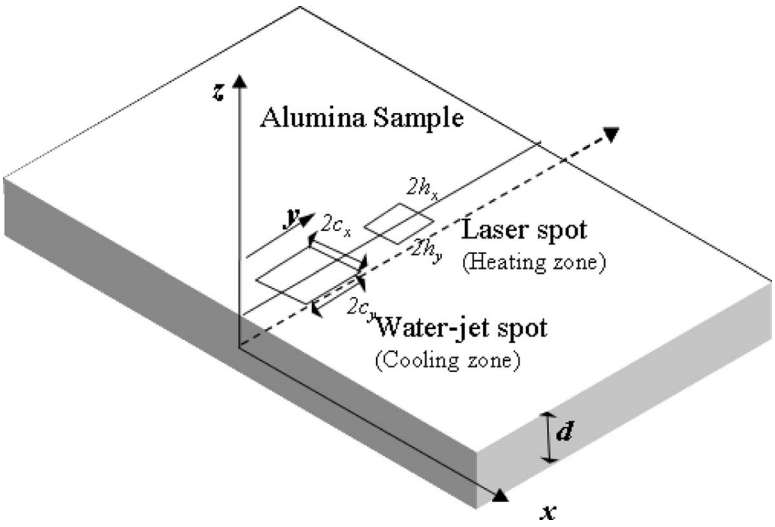

Fig. 3 Orientation of the axes with respect to the workpiece. The *y*-axis represents the cutting direction.

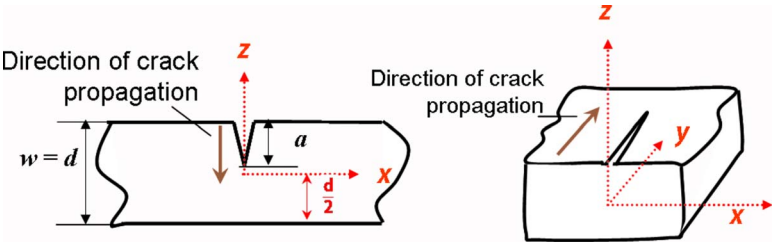

Fig. 4 (*a*) **Plane strain cracking and** (*b*) **crack channeling**

$$k\frac{\partial T}{\partial z}_{z=d/2} = k\frac{\partial T}{\partial x}_{x=\pm a} = k\frac{\partial T}{\partial y}_{y=b} = -h(T-T_A)$$

$$\frac{\partial T}{\partial z}_{z=-d/2} = \frac{\partial T}{\partial y}_{y=0} = 0 \quad \text{(insulated boundary condition)} \tag{2}$$

The transient temperature distribution is determined using a Green's function approach

$$T(x,y,z,t) = \int_0^t \int_0^b \int_{-a}^a q(x_0,y_0,t_0,I_h,I_c)\,\theta(x,x_0,y,y_0,z,t,t_0)dx_0dy_0dt_0 + T_0 \tag{3}$$

where $\theta(x,x_0,y,y_0,z,t,t_0)$ is the solution to the associated problem

$$c_p\rho\frac{\partial T}{dt} = k\nabla^2 T + \delta(x-x_0)\delta(y-y_0)\delta\left(z-\frac{d}{2}\right)\delta(t-t_0) \tag{4}$$

Eigenfunction expansions along the x, y, z coordinates are utilized to determine the series representation of Green's function θ

$$\theta(x,x_0,y,y_0,z,t,t_0) = \frac{\kappa}{k}\sum_{n=1}^{\infty}\exp(-\kappa\omega_n^2(t-t_0))\cos(\omega_n x)\cos(\omega_n x_0) \cdot \sum_{m=1}^{\infty}\exp(-\kappa\xi_m^2(t-t_0))\cos(\xi_m y)\cos(\xi_m y_0) \cdot \sum_{l=1}^{\infty}\exp(-\kappa\psi_l^2(t-t_0))\cos(\psi_l d)\cos(\psi_l(z+d/2))\cdot H(t-t_0) \tag{5}$$

where ω_n, ξ_m, and ψ_l are the eigenvalues along the x, y, z directions, and κ is thermal diffusivity.

Nonuniform heating and cooling of the specimen leads to the development of thermal stresses in the specimen [20]. Uncoupled quasistatic thin plate analysis is used to determine the resulting thermal stress fields. For the sake of brevity, only the stress component (σ_{xx}) along the x axis that results in the opening or closing of microcracks is discussed. Similar analysis may be utilized to calculate the other components of stress. Normal stress along the x axis of the free plate subjected to the temperature distribution, $T(x,y,z,t)$ is

$$\sigma_{xx} = \frac{1}{1-\nu}\left(-\alpha ET + \frac{1}{d}((1-\nu)N_x + N_T)\right) - \frac{12zD}{d^3}\left(\frac{\partial^2 w}{\partial x^2} + \frac{\partial^2 w}{\partial y^2}\right) \tag{6}$$

where ν is Poisson's ratio, α is the coefficient of thermal expansion, E is Young's modulus, N_x is the in-plane force per unit length, D is the bending rigidity of the plate per unit length, w is the out-of-plane displacement along the z direction, and N_T is calculated as

$$N_T = \alpha E\int_{-d/2}^{d/2} T dz \tag{7}$$

The in-plane forces per unit length are determined from the in-plane equilibrium equations while the out-of-plane displacement field is determined from the equilibrium of moments and out-of-plane forces.

The thermomechanical analysis of laser/waterjet machining is based on the following assumptions: physical and thermal properties of materials and surface heat transfer coefficients are assumed to be independent of temperature, and uncoupled quasistatic thermoelasticity is used to describe material response. In addition, only a small volume of the material is expected to undergo melting, evaporation, and resolidification during LWJ machining, and it is assumed that this small volume has minimal influence on thermal stress development in the rest of the specimen. Consequently, the process of material melting, evaporation, and solidification are not included in this analysis.

3.2 Computational Procedure for Crack Driving Forces. During LWJ machining, laser irradiation not only heats the surface but also causes localized damage that results in crack nucleation and propagation during the waterjet quenching. Laser-induced damage can result into two possible crack configurations—edge crack toward the center of the plate or channeling crack along the surface—schematically represented in Fig. 4. LWJ machining is represented through a two step analysis: (1) at the beginning of the cut when there are no preexisting cracks in the workpiece, plain strain analysis of edge crack is utilized to approximate the initial cut depth; and (2) subsequent analysis of the channeling crack is utilized to approximate the propagation of the initiated cut along the laser path.

Thermal stress fields are used to compute the crack driving forces corresponding to different crack lengths for both crack configurations. The stress intensity factors for plane strain edge cracks are calculated using the weight function method for Mode I loading of the crack in the x-z plane [21]. The weight functions for different crack lengths were computed using a finite element package, ABAQUS (Providence, RI).

The channeling of an edge crack is a three-dimensional process and for steady state crack extension, it is assumed that edge crack will channel at a fixed depth, with a constant tip shape and constant release rate. Hence, the driving force for a steady state crack growth is determined from the average energy release rate over the depth of the channeling crack front [17]

$$G_t = \frac{1}{a}\int_0^a G_p(a')da' \tag{8}$$

The stress intensity factor calculated for plane strain cracks are used in the above equation to compute the energy release rate for channeling cracks of different depths.

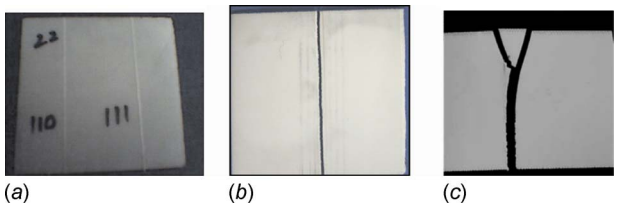

Fig. 5 (*a*) Photographs of scribing, (*b*) controlled, and (*c*) uncontrolled fracture

4 Experimental Results

The samples obtained from cutting experiments were categorized on the basis of the observed fracture response into scribing, controlled separation, and uncontrolled fracture, as shown in Fig. 5. Fracture behavior at different line energy (laser energy per unit length) inputs is plotted in Fig. 6(*a*) for the two laser spot sizes. Cutting experiments with a focused spot size of 0.2 mm results in uncontrolled cracking for high line energy values and controlled separation or scribing for only a narrow range of line energy values. In contrast, the 0.6 mm spot size resulted in controlled separation over a wide range of line energy values and a sharp transition from scribing to controlled separation at a line energy value of 4.00 J/mm. Observed fracture behaviors are also plotted as a function of surface energy density (laser energy per unit irradiated area) in Fig. 6(*b*). At lower values of surface energy density samples either undergo scribing or controlled separation but at larger magnitudes of surface energy density, samples undergo uncontrolled cracking. These experiment results indicate that both line energy and surface energy density are important parameters in determining the controlled separation of alumina samples undergoing LWJ machining. Thus, line energy determines the transition from scribing to fracture for larger spot sizes while the surface energy density determines the transition from controlled cracking to uncontrolled cracking.

Depth of crack induced in the scribed samples during LWJ machining was also measured to compare with theoretical predictions of crack growth. For this purpose, a low surface tension dye was applied and allowed to dry on the top surface. Subsequently, the samples were broken along the scribed crack and examined

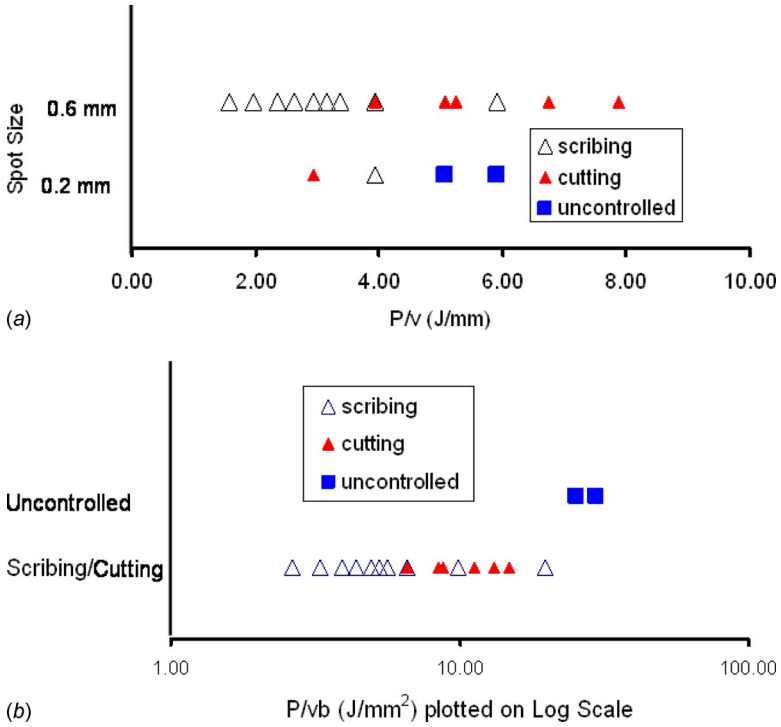

Fig. 6 (*a*) LWJ cutting of alumina for different spot sizes at 2.07 MPa of water pressure and (*b*) LWJ cutting results at 2.07 MPa of water pressure

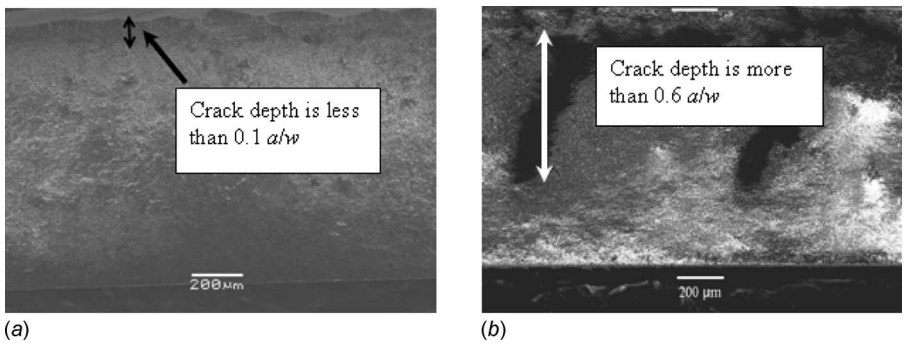

Fig. 7 SEM image of dye penetration in broken scribed specimens: (*a*) low line energy scribing and (*b*) high line energy scribing

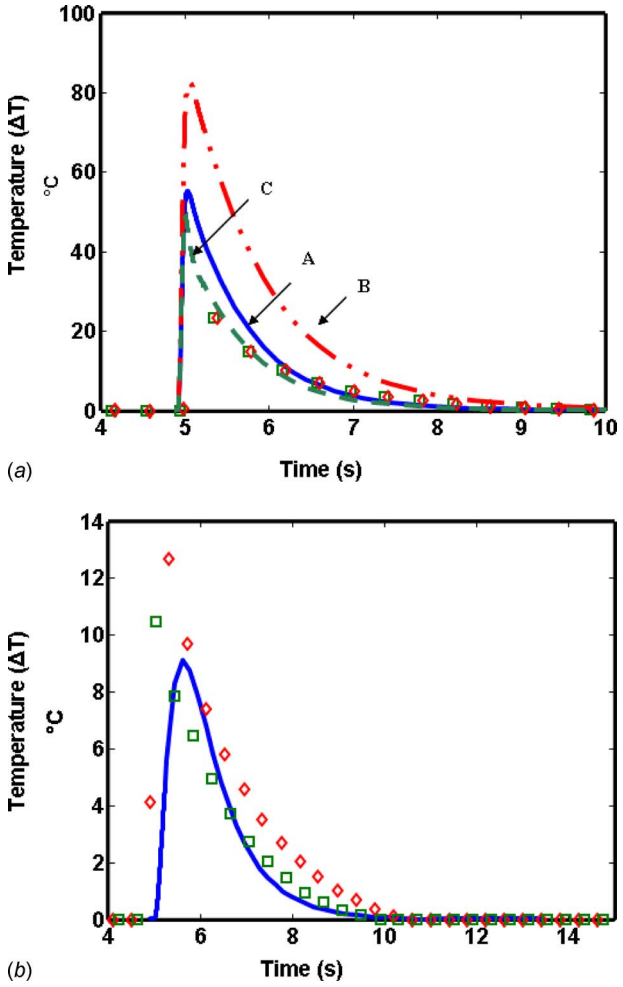

Fig. 8 Comparison of experimental measurements and numerical prediction of temperature during LWJ machining: (*a*) temperature measured at 1 mm from the cutting path (◇ and □ markers) and numerical predictions for three different conditions (curves A, B, and C); and (*b*) measured temperature (◇ and □ markers) and numerical predictions (curve A) at a 2 mm offset from the cutting path

with the help of scanning electron microscope (SEM). Typical SEM images of cracked samples scribed at low (3 J/mm) and high line energy values (4 J/mm) are presented in Figs. 7(*a*) and 7(*b*), respectively. The dye covered surfaces appear darker than uncovered alumina surfaces due to a difference in atomic numbers and hence can be used to identify the scribed crack depth. In the samples scribed at low line energy values, dye penetration and depth of scribed crack are consistently found to be less than 100 μm or less than 10% of the sample thickness (Fig. 7(*a*)). In the samples scribed at high line energy values, maximum dye penetration is found to be approximately 600–700 μm or about 60–70% of the sample thickness. For the deeper cracks dye seems to have flown along the crack in the form of fingers, which may be attributed to the small crack opening to depth ratio. Hence, we have approximated the scribed crack depth at high line energy values to be the maximum dye penetration at about 60–70% of the sample thickness.

Representative temperature histories recorded at points that are at distances of 1 mm and 2 mm from the cutting line during LWJ machining at a laser power of 150 W, spot size of 0.6 mm, and cutting velocity of 29.6 mm/s (70 in./min) are plotted in Figs. 8(*a*) and 8(*b*), respectively. Temperature values measured at opposite sides of the laser path match each other within $\pm 2^\circ$C.

Table 1 Properties of alumina used in the analysis

Density (kg/m^3)	Thermal conductivity (W/m K)	Specific heat capacity (J/kg K)	Young's modulus (GPa)	Thermal coefficient of expansion (/K)
3720	5	1320	330	8.5×10^{-6}

5 Analytical Predictions and Discussion

5.1 Temperature and Thermal Stress Distributions. Transient temperature and stress distributions in the alumina specimen were evaluated for a range of process parameters. In the analytical model, quantities such as specimen dimensions, cutting velocity, laser spot size, waterjet area, separation between the laser beam and waterjet, were chosen to exactly match the experimental conditions. Material properties used for the alumina specimen are given in Table 1 and are assumed to be temperature independent. Intensity of the heat flux incident over the laser spot was determined from

$$I_h = a_s \frac{4P}{\pi b^2} \tag{9}$$

where P represents laser power, b represents the diameter of the laser beam spot used in LWJ machining, and a_s represents the absorption coefficient for the alumina specimen. Alumina is known to exhibit high absorption of CO_2 laser radiation (on the order of 95%) [22,23]. It was assumed that $a_s=0.72$, i.e., 72% of the laser incident energy is absorbed in the sample based on approximating 5% losses in the laser optics and 20% losses due to the presence of water vapor and 95% absorptance of CO_2 laser beam at 10.6 μm wavelength for alumina.

In the numerical model, waterjet quenching of the laser heated area is approximated using a heat sink along with convective cooling over the top surface because the large temperature variation over the sample generates nonuniform convection involving both forced convection due to water flow and pool boiling over the cutting path (water vapor/mist formation was observed during the experiments). The cooling intensity of heat sink and the convection heat transfer coefficient were estimated using the following two assumptions: (1) waterjet quenching will rapidly reduce the temperature of the laser heated area to room temperature; and (2) flow of water over the sample will result in forced convection (with coefficient value between 50 W/m^2 K and 20,000 W/m^2 K [24,25]. In addition, analytical predictions were compared against measured temperature histories to obtain the effective sink intensity and heat transfer coefficient over the surface.

Temperature distribution is computed for a finite area of 0.04×0.1 m^2 for the boundary conditions mentioned in Eq. (3), using 50 eigenvalues along the x and z axes and 400 eigenvalues along the y axis. Number of eigenvalues along each direction was chosen on the basis of numerical convergence studies to ensure that the increase in the number of eigenvalues produces an insignificant change in the predictions of the maximum tensile stress on the surface during waterjet quenching. Comparison of numerical predictions for different combinations of laser power and cutting velocity showed that the predicted temperature and thermal stresses were approximately the same for a fixed line energy value. Hence for the sake of brevity, all the results are presented as a function of line energy rather than different laser power and cutting velocity values.

Predictions at 1 mm from the cutting path for three different cooling intensities, and convective heat transfer coefficients are compared with experimental measurements during LWJ machining at a line energy of 5 J/mm for a spot size of 0.6 mm in Fig. 8(*a*). Case A corresponds to a cooling intensity (I_c) of 25×10^6 W/m^2 and convective coefficient of 10×10^3 W/m^2 K, Case B corresponds to a cooling intensity (I_c) of 25×10^6 W/m^2

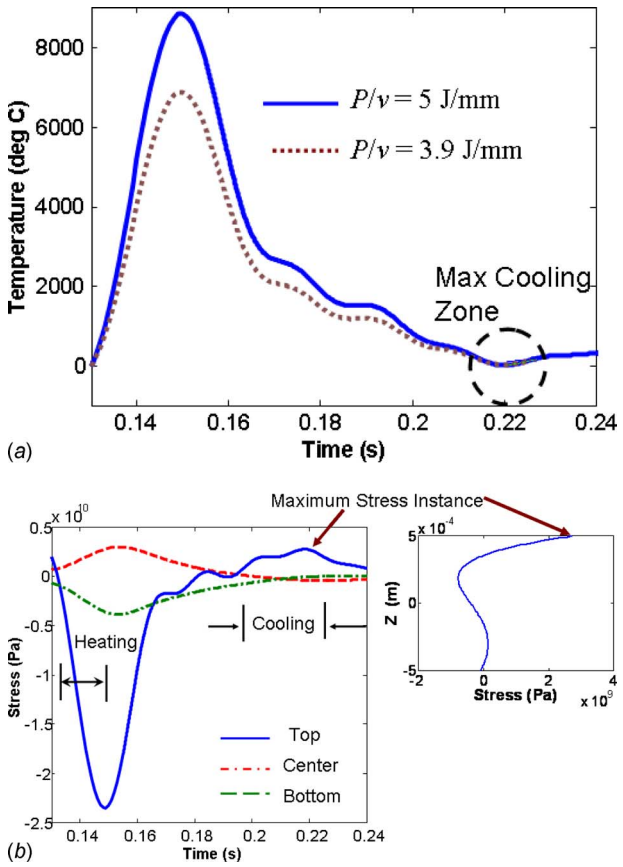

Fig. 9 (*a*) **Temperature plot at *x*=0 m, and *y*=0.004 m at various line energies and** (*b*) **stress plot at *x*=0 m, and *y*=0.004 m at various *z* with the inset showing the stress across the thickness**

and convective coefficient of 6×10^3 W/m^2 K, and Case C corresponds to a cooling intensity (I_c) of 50×10^6 W/m^2 and convective coefficient of 10×10^3 W/m^2 K. A comparison of the three curves reveals that the heat transfer coefficient determines the peak temperatures while the cooling intensity determines the rate of cooling during the quenching process. Best approximation of the experimental data is achieved in Case C but this choice of cooling intensity results in quenching of the material on the cutting path to temperatures significantly below the waterjet temperature. As a result, the value of cooling intensity in Case A was chosen to approximate the LWJ machining for a line energy of 5 J/mm because it ensures quenching of the material on the cutting path to room temperature and produces reasonable agreement with the experimentally measured temperature at a distance of 1 mm and 2 mm from the cutting path, as shown in Figs. 8(*a*) and 8(*b*), respectively.

Similar procedure was utilized to identify the cooling intensity that approximates the waterjet quenching at other line energy values. Predictions of temperature history at a point along the cutting path corresponding to two different line energy values (3.9 J/mm and 5 J/mm) are plotted in Fig. 9(*a*)). The peak temperatures are predicted to be higher than the melting temperature as the model considers conduction only. Phase transformations in the form of melting, vaporization, and resolidification are ignored in this analysis and as a result peak temperature predictions for points along the laser path are higher than the vaporization temperature. It is appropriate to note that our main focus will remain on the prediction of tensile stresses, which occurs during cooling, rather than the compressive stresses during heating, and hence the melting and vaporization effect can be ignored. Also, the size of such high-temperature zones are small (~70 μm) and are shown in the experimental results discussed in Ref. [5]. However, these very high temperatures do not affect the calculation of crack driving forces and subsequent conclusion. It is important to note that peak temperatures and associated compressive stresses do not influence the tensile stresses generated during waterjet quenching, and hence our assumption of ignoring phase transformations is justified and our model successfully captures the essential mechanisms governing material separation during LWJ machining.

Predictions of in-plane stress component, σ_{xx}, for LWJ machining at a line energy of 3.9 J/mm at the top, middle, and bottom surfaces at a point along the laser path are plotted in Fig. 9(*b*). Arrival of the laser spot on the top surface leads to rapid heating and development of compressive stresses. Quenching of the laser heated area with the waterjet results in the development of large tensile stresses on the top surfaces while the middle and bottom surfaces are relatively unstressed. Through-the-thickness stress distribution at the instance of maximum tensile stress on the top surface is plotted in the inset shown in Fig. 9(*b*). This large in-plane tensile stress will result in the propagation of cracks that lead to scribing or splitting of the specimen.

Our solution approach for both temperature and stress calculations relies on the summation of eigenfunctions for temperature and stress computations. The number of eigenvalues along each direction was chosen on the basis of numerical convergence studies to ensure that the increase in the number of eigenvalues produces an insignificant change in the predictions of the maximum tensile stress on the surface during waterjet quenching. Eigenfunction expansion provides a simple form for the temperature and stresses but suffers from very slow convergence in resolving large gradients associated with changes in the sign of the surface heat flux from laser heating to waterjet cooling. The slow rate of convergence leads to a wavy profile for the temperature between the laser heating and subsequent cooling. Increasing the number of eigenfunctions in the temperature and stress calculations leads to smoother curves but leads to extremely large computational times. However, the increase in eigenvalues has no effect on the magnitude of the maximum tensile stress that occurs away from this undulating profile. Since the focus of this paper is to determine the crack propagation driven by the maximum tensile stress, convergence studies were based on the magnitude of the maximum tensile stress rather than the shape of overall temperature curves.

5.2 Crack Driving Forces. Predicted stress histories were used to calculate the driving forces for plane strain and channeling crack configurations. Crack driving forces reach the maximum at the instant when the top surface is subjected to maximum tensile stress during waterjet quenching (shown in Fig. 9(*b*)). The computed stress intensity factors for plane strain cracks at that instant are plotted as a function of crack length for four different processing parameters in Fig. 10. Computed energy release rates for channeling cracks are plotted as a function of the crack depth for the same processing conditions in Fig. 11. First three predictions correspond to LWJ machining with a laser spot size of 0.6 mm and line energies of 3.0 J/mm, 3.9 J/mm, and 5.0 J/mm, respectively. First two line energy line values resulted in scribing while the third case corresponds to the controlled separation of alumina specimens. The fourth prediction corresponds to LWJ machining with A spot size of 0.2 mm and line energy of 5.0 J/mm, which results in high surface energy density (33 J/mm^2) and uncontrolled cracking. In all the cases, stress intensity factor (K_I) and energy release rates (G) are highest for cracks that are approximately 0.1 times the thickness due to the large tensile stresses induced on the top surface during quenching. K_I and G rate decrease as the crack becomes longer and reach a minimum for cracks that are roughly 0.5–0.6 times the thickness due to the compressive stresses induced in the middle portion of the material (Fig. 9(*b*)). In addition, the increase in both the line energy and the surface energy density leads to an increase in the computed values

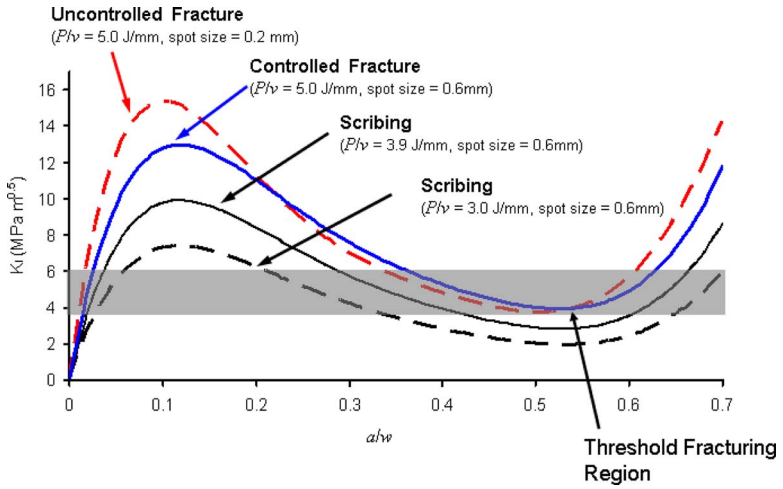

Fig. 10 K_I **at various** a/w ($a \equiv$ **crack length and** $w \equiv$ **thickness) ratios**

of K_I and G. For the same line energy value, LWJ machining with a smaller spot size results in higher values of K_I and G for cracks shorter than 0.4 times the thickness.

Numerical predictions of K_I and G are also compared to alumina's fracture toughness (K_{Ic}) and critical energy release rate (G_c) in Figs. 10 and 11, respectively, in order to estimate the cut depth at the start of LWJ machining, as well as the equilibrium depth of the channeling crack for each processing condition. As shown in the Fig. 10, K_I for cracks shorter than 0.25–0.45 times the thickness is larger than K_{Ic} of the alumina for the given range of line energy values. Thus, the initial cut depth will be in the range of 0.25–0.45 times thickness. In addition, G for channeling cracks of these depths is higher than G_c for the processing parameters considered in Fig. 11, therefore the initial cracks are expected to propagate along the laser path. However, these predictions of cut depth are most appropriate for machining situations where laser irradiation-induced damage is only confined to the top surface of the specimen. These predictions cannot be directly compared to experimental observations of through-cuts where laser radiation is incident over the specimen boundary resulting in damage and subsequent cracking across the whole thickness during waterjet quenching. As a result, the equilibrium depth of a channeling crack is most appropriate for determining the LWJ induced cut depth in the current experiments.

The maximum value of G increases with the increase in line energy (P/v) for a fixed spot size of 0.6 mm, as shown in Figs. 10 and 11, respectively (see controlled fracture ($P/v=5$ J/mm) and scribing ($P/v=3.9$ J/mm, and $P/v=3.0$ J/mm)). At line energy values lower than 3.0 J/mm, G for all crack lengths is lower than G_c hence scribing with a crack depth less than 0.1 times the thickness is observed (see Fig. 7(a)). For line energy values between 3.0 J/mm and 3.9 J/mm, G for short cracks is greater than G_c, but for cracks approximately 0.6 times the thickness G is lower than G_c and as a result, scribing with a crack depth 0.6 times the thickness is observed. As the line energy values are further increased, the G value for all crack lengths becomes greater than G_c resulting in channeling of through-the-thickness cracks or material separation. In order to verify this hypothesis, magnitudes of predicted minimum G for channeling cracks are plotted as a function of line energy in Fig. 12 for a fixed spot size of 0.6 mm. Comparison of the magnitude of the minimum energy release rate with the range of G_c indicates that transition from scribing to material separation should occur for a line energy value between 3.4 J/mm and 4.4 J/mm. During the cutting experiments, the transition from scribing to material separation is observed at a line energy value

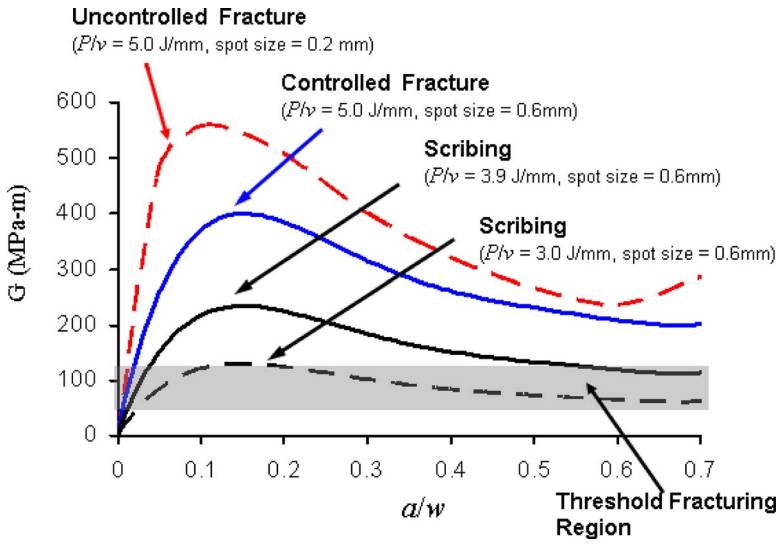

Fig. 11 G **curve at various** a/w ($a \equiv$ **crack length and** $w \equiv$ **thickness) ratios**

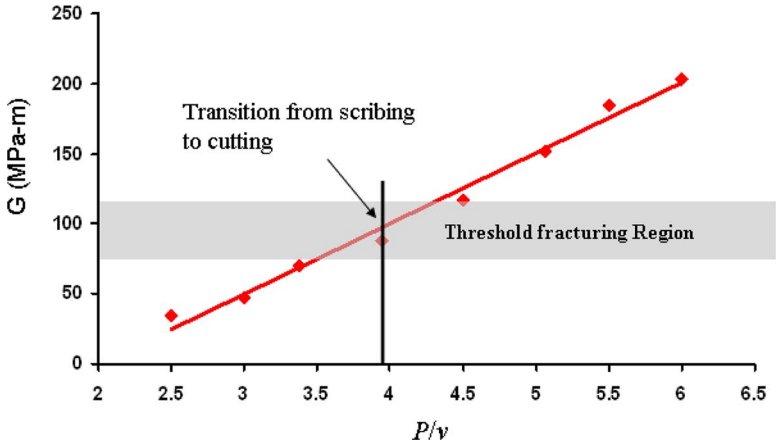

Fig. 12 Minimum energy release rates plotted as a function of line energy for a spot size of 0.6 mm

of 3.9 J/mm and this excellent agreement between numerical predictions and experimental observations validates the hypothesis. Thus, the magnitude of minimum energy release rate may be used for predicting the transition from scribing to material separation during LWJ machining.

During material separation, the transition from controlled separation to uncontrolled cracking depends on the surface energy density. As seen in Fig. 11, the G for shorter cracks (smaller a/w) is much larger in the case of high surface energy density (uncontrolled fracture (33 J/mm^2)). Previous work [26] on the stability of crack path has shown that an increase in driving forces can result in transition from a single straight crack to undulating and branched crack propagation. In addition, the extent of surface damage during laser irradiation is expected to scale in proportion to surface energy density. Therefore, the increase in surface damage and larger driving forces for smaller cracks are expected to result in a transition from controlled separation to uncontrolled cracking. Based on the experimental observations, surface energy density of 33 J/mm^2 is identified as the critical value at which transition from controlled separation to uncontrolled cracking takes place.

Number of numerical simulations of LWJ machining at different line energy and surface energy values are carried out to create a map shown in Fig. 13 that relates the process parameter to the expected fracture characteristics of alumina specimens. Minimum G for channeling cracks are used to identify the transition from scribing to material separation, and the critical value of surface energy density is utilized to predict transition from controlled separation to uncontrolled cracking. Line energy values greater than 20 J/mm will result in a "melt and blow" mode of material separation in alumina [24] and hence are the upper limit of line energy values in LWJ machining. Experimental observations at laser spot sizes of 0.2 mm and 0.6 mm and numerical predictions at a spot size of 0.4 mm are also plotted on the process map. The process map will serve as a useful tool for identifying appropriate LWJ parameters for cutting or scribing of alumina.

6 Conclusions

The analytical model and experimental results presented in this paper clearly demonstrate that a fracture mechanics based approach can be used to design hybrid machining processes for brittle materials. A hybrid laser/waterjet machining process is investigated for cutting alumina specimen. Cutting experiments were conducted to observe fracture characteristics of alumina samples. Numerical models were developed to predict temperature, stress field, and driving forces for cracks that result in scribing and separation of the workpiece. Comparison of experimental and numerical results indicated that the critical value of driving force for channeling cracks determines the transitions between scribing to material separation, whereas a critical value of surface energy density determines the transition from controlled separa-

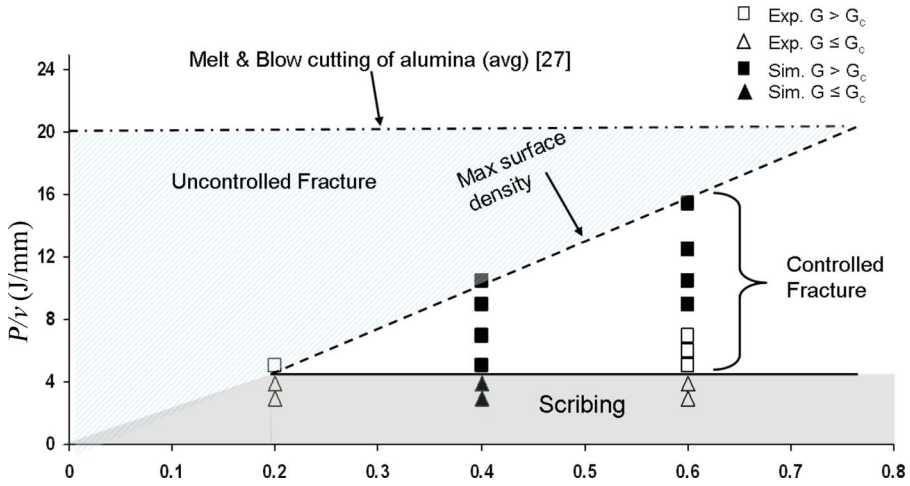

Fig. 13 Graph relating process parameters and fracture characteristics [27]

tion to uncontrolled cracking of the workpiece. Based on these observations, a map is created to relate process parameters to fracture characteristics of alumina specimens.

Acknowledgment

The authors gratefully acknowledge the financial support for this research provided by the U.S. National Science Foundation under the Grant No. DMI-0522788.

References

[1] Hashish, M., 1984, "Cutting With Abrasive Waterjets," Mech. Eng. (Am. Soc. Mech. Eng.), **106**, pp. 60–69.
[2] Gudimetla, P., Wang, J., and Wong, W., 2002, "Kerf Formation Analysis in the Abrasive Waterjet Cutting of Industrial Ceramics," J. Mater. Process. Technol., **128**, pp. 123–129.
[3] Schroede, Dh., and English, F. L., 1972, "Comparison of Strength of Alumina Substrates for Different Separation Techniques," IEEE Transactions on Parts Hybrids and Packaging, **PHP8**, pp. 4–6.
[4] Huang, H., and Liu, Y. C., 2003, "Experimental Investigations of Machining Characteristics and Removal Mechanisms of Advanced Ceramics in High Speed Deep Grinding," Int. J. Mach. Tools Manuf., **43**, pp. 811–823.
[5] Kalyanasundaram, D., Shehata, G., Neumann, C., Shrotriya, P., and Molian, P., 2008, "Design and Validation of a Hybrid Laser/Water-Jet Machining System for Brittle Materials," J. Laser Appl., **20**, pp. 127–134.
[6] Hong, L., and Li, L. J., 1999, "A Study of Laser Cutting Engineering Ceramics," Opt. Laser Technol., **31**, pp. 531–538.
[7] Shehata, G., Molian, P. A., Bastawros, A., and Shrotriya, P., 2007, "Surface Finish and Flexural Strength of CO_2 Laser-Cut Alumina by Evaporative and Thermal Stress Fracture Modes," Trans. North Am. Manuf. Res. Inst. SME, **35**, pp. 391–400.
[8] Kalyana-Sundaram, D., Wille, J., Shrotriya, P., and Molian, P., 2008, "CO_2 Laser/Waterjet Machining of Polycrystalline Cubic Boron Nitride," Trans. North Am. Manuf. Res. Inst. SME, **36**, pp. 517–524.
[9] Lumley, R. M., 1969, "Controlled Separation of Brittle Materials Using a Laser," Am. Ceram. Soc. Bull., **48**, pp. 850–854.
[10] Tsai, C. H., and Liou, C. S., 2003, "Fracture Mechanism of Laser Cutting With Controlled Fracture," ASME J. Manuf. Sci. Eng., **125**, pp. 519–528.
[11] Tsai, C. H., and Chen, C. J., 2003, "Formation of the Breaking Surface of Alumina in Laser Cutting With a Controlled Fracture Technique," Proc. Inst. Mech. Eng., Part B, **217**, pp. 489–497.
[12] Segall, A. E., Cai, G., Akarapu, R., Romasco, A., and Li, B. Q., 2005, "Fracture Control of Unsupported Ceramics During Laser Machining Using a Simultaneous Prescore," J. Laser Appl., **17**, pp. 57–62.
[13] Li, K., and Sheng, P., 1995, "Plane-Stress Model for Fracture of Ceramics During Laser Cutting," Int. J. Mach. Tools Manuf., **35**, pp. 1493–1506.
[14] Barnes, C., Shrotriya, P., and Molian, P., 2007, "Water-Assisted Laser Thermal Shock Machining of Alumina," Int. J. Mach. Tools Manuf., **47**, pp. 1864–1874.
[15] Akapura, R., Li, B., and Segall, A. E., 2004, "A Thermal Stress Failure Model for Laser Cutting and Forming Operations," Journal of Failure Analysis and Prevention, **4**, pp. 51–62.
[16] Lu, T. J., and Fleck, N. A., 1998, "The Thermal Shock Resistance of Solids," Acta Mater., **46**, pp. 4755–4768.
[17] Zhao, L. G., Lu, T. J., and Fleck, N. A., 2000, "Crack Channelling and Spalling in a Plate Due to Thermal Shock Loading," J. Mech. Phys. Solids, **48**, pp. 867–897.
[18] Olagnon, C., Chevalier, J., and Pauchard, V., 2006, "Global Description of Crack Propagation in Ceramics," J. Eur. Ceram. Soc., **26**, pp. 3051–3059.
[19] Elperin, T., Kornilov, A., and Rudin, G., 2000, "Formation of Surface Microcrack for Separation of Nonmetallic Wafers Into Chips," ASME J. Electron. Packag., **122**, pp. 317–322.
[20] Boley, B. A., and Weiner, J. H., 1997, *Theory of Thermal Stresses*, Dover, Mineola, NY.
[21] Tada, H., Paris, P. C., and Irwin, G. R., 1985, *Stress Analysis of Cracks Handbook*, Del Research, St. Louis, MI.
[22] Khelkhal, M., and Herlemont, F., 1992, "Determination of Effective Optical-Constants of Infrared CO_2 Wave-Guide Laser Materials," Appl. Opt., **31**, pp. 4175–4181.
[23] Moorhouse, C. J., Villarreal, F., Wendland, J. J., Baker, H. J., Hall, D. R., and Hand, D. P., 2005, "CO_2 Laser Processing of Alumina (Al_2O_3) Printed Circuit Board Substrates," IEEE Trans. Electron. Packag. Manuf., **28**, pp. 249–258.
[24] Incropera, F. P., and DeWitt, D. P., 1996, *Introduction to Heat Transfer*, 3rd ed., Wiley, New York.
[25] Ashby, M. F., 2001, *Materials Selection in Mechanical Design*, Butterworth-Heinemann, Oxford, England.
[26] Yang, B. and Ravi-Chandar, K., 2001, "Crack Path Instabilities in a Quenched Glass Plate," J. Mech. Phys. Solids, **49**, pp. 91–130.
[27] Steen, W., 2003, *Laser Materials Processing*, 3rd ed., Springer, New York.